Journal of Materials Chemistry A



PAPER View Article Online



Cite this: DOI: 10.1039/c9ta01249d

Wearable high-dielectric-constant polymers with core-shell liquid metal inclusions for biomechanical energy harvesting and a self-powered user interface†

Shengjie Gao,^{ab} Ruoxing Wang,^{ab} Chenxiang Ma,^{abc} Zihao Chen,^d Yixiu Wang,^{ab} Min Wu,^{ab} Zhiyuan Tang,^c Ning Bao,^e Dong Ding, ^{for the foliation of the foliation o}

Deformable energy devices capable of efficiently scavenging ubiquitous mechanical signals enable the realization of self-powered wearable electronic systems for emerging human-integrated technologies. Triboelectric nanogenerators (TENGs) utilizing soft polymers with embedded additives and engineered dielectric properties emerge as ideal candidates for such applications. However, the use of solid filler materials in the state-of-the-art TENGs limits the devices' mechanical deformability and long-term durability. The current structural design for TENGs faces the dilemma where the enhanced dielectric constant of the TENG's contact layer leads to an undesirable saturation of the surface charge density. Here, we present a novel scheme to address the above issues, by exploring a liquid-metal-inclusion based TENG (LMI-TENG) where inherently deformable core—shell LMIs are incorporated into wearable high-dielectric-constant polymers. Through a holistic approach integrating theoretical and experimental efforts, we identified the parameter space for designing an LMI-TENG with co-optimized output and mechanical deformability. As a proof of concept, we demonstrated an LMI-TENG based wireless media control system for a self-powered user interface. The device architecture and design scheme presented here provide a promising solution towards the realization of self-powered human-integrated technologies.

Received 31st January 2019 Accepted 22nd February 2019

DOI: 10.1039/c9ta01249d

rsc.li/materials-a

Introduction

The capability of functional devices to scavenge environmental energy through sustainable pathways is expected to enable exciting opportunities in self-powered micro-/nano-systems for

emerging technologies,1-5 e.g., pervasive computing, advanced healthcare, human-machine interface, robotics, and the Internet of Things (IoT). An assortment of technologies has been developed to transform the otherwise wasted ambient mechanical energy into electrical power through mechanisms such as electrostatic, piezoelectric, and recently, triboelectric processes. Triboelectric nanogenerators (TENG) can efficiently harvest the ubiquitous mechanical energy for powering electronics and sensors, hinged on the principles of triboelectrification and electrostatic induction. 6-10 Ongoing TENG efforts primarily focus on augmenting power generation by increasing the surface area, engineering the physical/chemical properties of contacting surfaces and implementing practical applications. 11-13 Among these efforts, increasing the surface charge density through engineering the charge-trapping capabilities of the dielectric layers has been shown to be effective in boosting the TENG performance.14-18 Previous reports on such dielectric engineering suggest that the charge trapping ability of the contact layer (CL) in TENGs increases with the increased dielectric constant of the polymer layer,14 leading to improved TENG performance. Nevertheless, the secondary-phase additive materials used for dielectric engineering in the state-of-the-art TENGs are exclusively solid type14,19,20 with limited deformability. The inherently rigid nature

[&]quot;School of Industrial Engineering, Purdue University, West Lafayette, Indiana 47907, USA. E-mail: wenzhuowu@purdue.edu

^bFlex Laboratory, Purdue University, West Lafayette, Indiana 47907, USA

Department of Applied Chemistry, School of Chemical Engineering and Technology, Tianjin University, Tianjin, 300072, China

^aSchool of Electrical and Computer Engineering, Purdue University, West Lafayette, Indiana 47907. USA

^cSchool of Public Health, Nantong University, Nantong, Jiangsu, 226019, China ^LEnergy & Environment Science and Technology, Idaho National Laboratory, Idaho

^{*}Shenzhen Broadthink Advanced Materials Technologies Co., Ltd., Shenzhen, Guangdong, 518117, China. E-mail: wxwu@mail.ustc.edu.cn

^hDepartment of Chemistry & Biochemistry, University of California, Santa Barbara, CA 93106, USA. E-mail: fengrufan@ucsb.edu

Birck Nanotechnology Center, Purdue University, West Lafayette, Indiana 47907, USA

Regenstrief Center for Healthcare Engineering, Purdue University, West Laafayette,
Indiana 47907, USA

[†] Electronic supplementary information (ESI) available. See DOI: 10.1039/c9ta01249d

of these materials results in a severe compliance mismatch with the soft elastomer and issues such as undesirable stress concentrations and layer delamination, leading to deteriorated bulk deformability and long-term durability for wearable and stretchable applications. Moreover, recent studies suggest the saturation of surface charge density in the CL could significantly limit the TENG's performance. Under such a condition, the widely adopted electrostatic models fail to provide a fair evaluation of TENG performance and guidance for robust and optimal design.

To bridge these fundamental gaps and address technological issues, here we present the design and implementation of a liquid-metal-inclusion based TENG (LMI-TENG) with desirable deformability and optimized performance. The incorporation of deformable core-shell liquid metal/native oxide inclusions (Fig. 1a inset) into the TENG's silicone layers (Fig. 1c) enables synergistic engineering of the surface charge density at the material level, of the dielectric environment at the structure level, and of the boosted output power with desired deformability at the device level. Through a holistic integration of modeling and experiments, we demonstrate that the output performance of LMI-TENGs can be enhanced by 250% with an optimized, constant surface charge density for the CL when 50 wt% LMI is incorporated. We further reveal and identify for the first time the role of the surface leakage charge, a factor ignored by previous TENG studies, in the electrostatic process in the LMI-TENG. With these new fundamental understandings, we present a proof-of-concept demonstration of an LMI-TENG based wireless media control system for future human-integrated applications, e.g., a self-powered user interface. 13,25

The device structure of an LMI-TENG

Fig. 1a and c show the optical image and 3D schematics of an LMI-TENG, which consists of a layer of liquid metal embedded functional silicone (LMEFS) sandwiched by two Ecoflex® layers (thickness of each layer $\sim 100 \mu m$). The LMI-TENG has an indium tin oxide (ITO) back electrode (BE) and a grounded aluminum reference electrode (RE). The LMEFS layer was prepared by mixing different weight fractions (wt%) of Galinstan (a eutectic alloy with a composition ratio of Ga: 68.5%, In: 21.5%, and Tin: 10%) liquid metal particles (LMPs) with the Ecoflex silicone through a mechanical stirring process (ESI Fig. 1† and the Methods). Galinstan has a native oxide skin (\sim 1– 3 nm thick) which conformably covers each liquid metal particle once exposed to the air.26,27 The core-shell liquid metal/ native oxide structures facilitate the homogeneous dispersion of LMPs and eliminate the formation of a continuous conductive path among LMPs in the LMEFS.28 The two additional Ecoflex layers (Fig. 1c) ensure a constant surface charge density on the CL for LMI-TENGs with different wt% LMPs with the same mechanical inputs (detailed discussions are included in the section 'Characterization of the LMI-TENG's working performance'). This unique structural design in LMI-TENGS, different from previous TENGs,29-31 where the CL's surface charge density changes with the various dielectric constants, is critical for avoiding potential interference from the different surface charge densities due to the different LMP wt%, and helping develop a new fundamental understanding of the performance optimization in LMI-TENGs through synergistically engineering both the dielectric properties and the surface

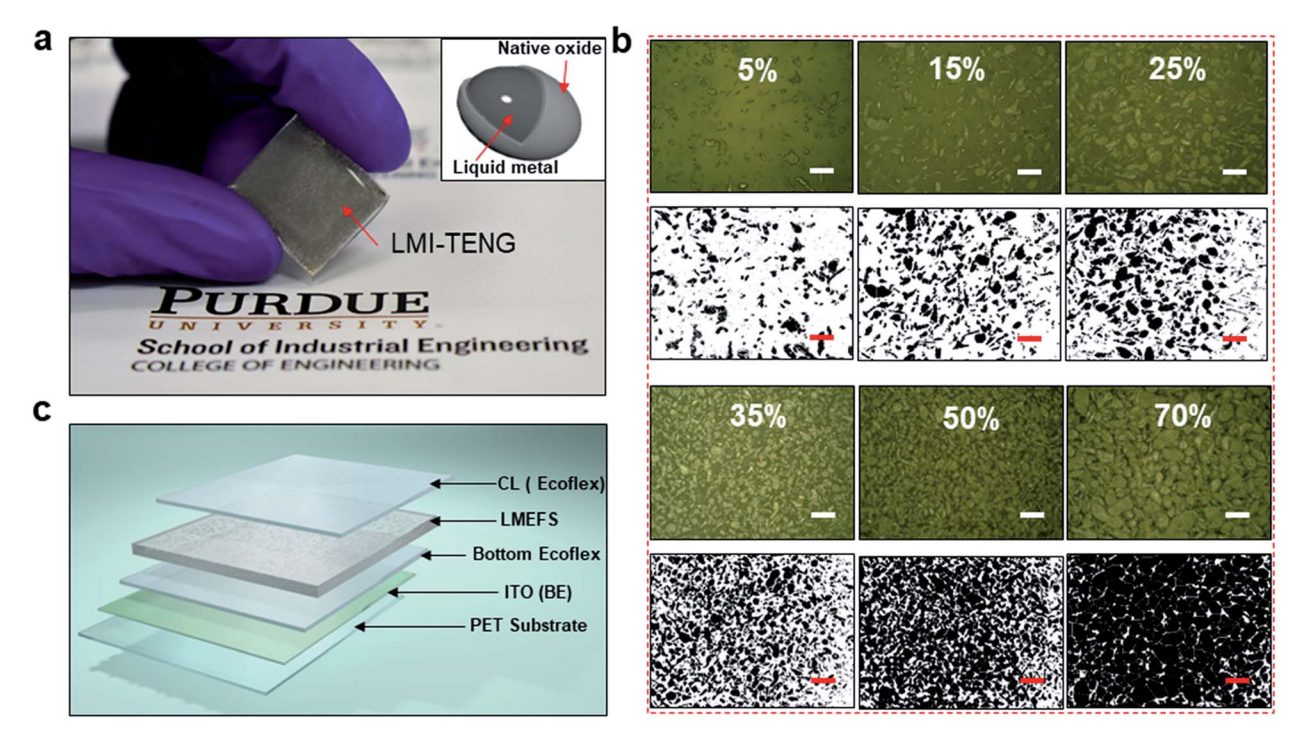


Fig. 1 Design of the LMI-TENG. (a) The optical image of the LMI-TENG. Inset: Schematic illustration of the microstructure of the liquid metal particle (LMP). (b) Top-down optical and processed images of the distribution of different wt% LMPs inside the silicone matrix. (c) 3D schematic illustration of the LMI-TENG's structure.

charge density. Fig. 1b shows a series of top-view optical images of the LMEFS layers containing different wt% of LMPs. The post-processed images (see the Methods) indicate that the shapes of the LMPs are ellipsoidal, with the primary radii ranging from 15 μm to 200 μm (ESI Fig. 2 and 6c†). The spatial distribution of LMPs within the LMEFS was visualized using 3D micro-computed tomography (Micro-CT) images of the sandwiched dielectric stacks (SDSs) (ESI Fig. 2†), showing a homogeneous dispersion of LMPs without forming a conductive percolation network, which is further confirmed by dielectric measurements (Fig. 2c). If a percolation network exists, the dielectric constant of the SDS should decrease significantly, 32 which is contrary to the result shown in Fig. 2c.

Characterization of the LMI-TENG's working performance

We experimentally characterized the open-circuit voltage $(V_{\rm oc})$, short-circuit current density $(J_{\rm sc})$ and short-circuit transferred charge density $(\sigma_{\rm sc})$ when different wt% LMPs were mixed with the LMEFS. The result (Fig. 2a(i)) shows that a 250% enhancement can be achieved in $V_{\rm oc}$ when the LMP concentration is increased from 0 wt% to 50 wt%. A similar enhancement is also observed for $J_{\rm sc}$ and $\sigma_{\rm sc}$ (Fig. 2a (ii)–(iii)). When the concentration of LMP is further increased (e.g., from 50 wt% to 70 wt%), the output performance starts to decrease (Fig. 2b), though the absolute values of $V_{\rm oc}$, $J_{\rm sc}$, and $\sigma_{\rm sc}$ are still more than twice

greater than those obtained for pristine TENGs without LMIs. ESI Fig. 3a† shows that the output power of the 50 wt% LMI-TENG reaches 13.95 mW m⁻², suggesting its potential to meet the power requirement for driving the operation of IoT devices.3 The ideal cycles of maximized energy output (CMEO),³³ a standard method to characterize the ideal maximum output performance of TENGs, for the LMI-TENG with different LMP wt% are compared in ESI Fig. 3b,† showing that the LMI-TENG can deliver a maximum output energy density of 1.33 mJ m⁻² per cycle. Dielectric measurements for different SDSs (ε_{SDS}) (Fig. 2c) are consistent with the electrical characterization result. When the LMP wt% increases from 0 wt% to 50 wt%, ε_{SDS} increases from 4.58 to 12.65, and starts to drop when the LMP wt% further increases to 70 wt%. The constant surface charge density for LMI-TENGs with different LMP wt% was confirmed by Kelvin Probe Force Microscope (KPFM) characterization (see the Methods). For each device, the surface potentials for both the aluminum electrode and the CL are measured (Fig. 2d and ESI Fig. 4†), showing no significant difference in the surface potential for CLs from different LMI-TENGs, indicating that the densities of surface charges on each CL remain constant as per our expectation.34 The constant surface charge density of CLs (Fig. 2d) is supposed to lead to a constant TENG output based on a previous theoretical report.24 However, the LMI-TENG's working performance varies with the different weight fractions

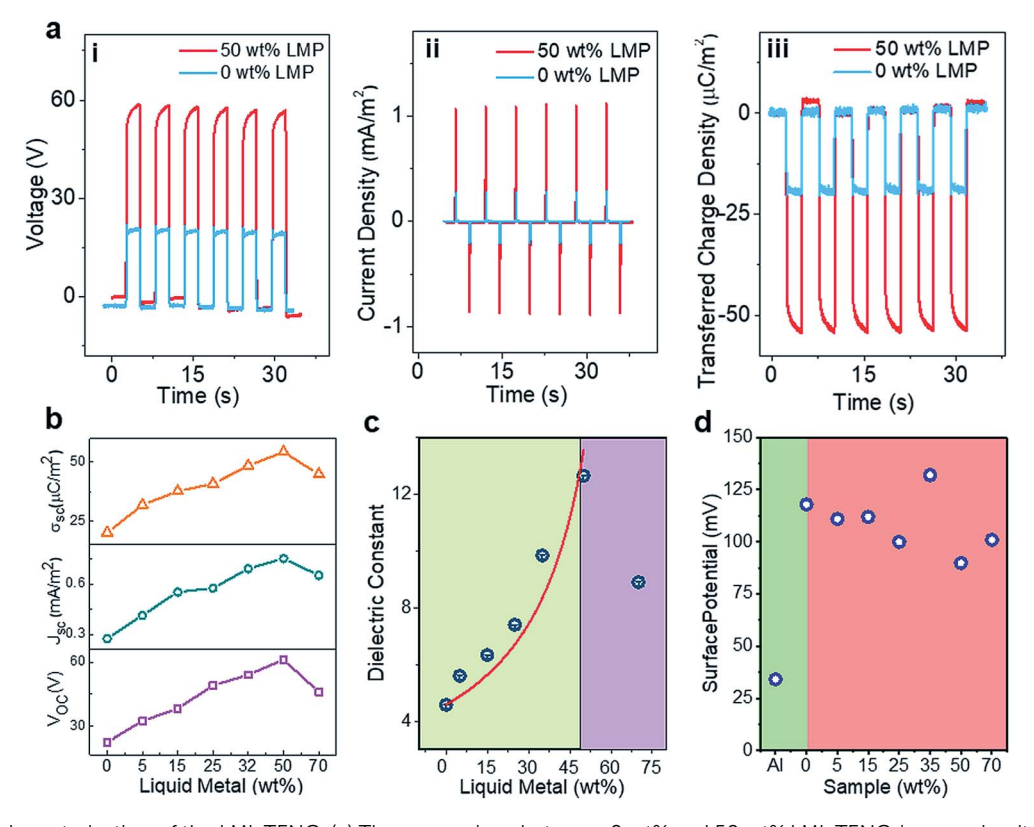


Fig. 2 Electrical characterization of the LMI-TENG. (a) The comparison between 0 wt% and 50 wt% LMI-TENGs' open-circuit voltage (i), short-circuit current density (ii) and short-circuit transferred charge density (iii). (b) Working performance summary of the LMI-TENG with different wt% of liquid metal. (c) The relationship between the dielectric constant of the SDS and weight fraction of LMPs. (d) The surface potential of the contact layer on different types of SDS measured by KPFM.

of LMP (Fig. 2b), indicating that a deeper understanding of the working mechanism of TENGs is necessary.

Dielectric engineering and analysis of SDSs

To better understand the relationship between the LMP wt% and the dielectric constant of SDSs for revealing the operation mechanism of LMI-TENGs, we apply percolation theory to quantitatively analyze the dependence of $\varepsilon_{\rm SDS}$ on the LMP wt%. Given that the SDS can be considered as a binary-phase system, where Ecoflex silicone is the matrix material and LMPs are the secondary-phase additives, the effect of LMP concentration on such a composite system's general physical properties can be expressed as:³²

Properties
$$\propto (f_c - f_i)^{-s'}$$
 (1)

where f_i is the relative fraction of the secondary phase, f_c is the percolation threshold related to the disappearance of the long-range, global connectivity of the second phase in the matrix, and s' is the critical exponent used to characterize the percolation transition.³⁵ When considering the dielectric properties, this relationship can be expressed as:³⁶

$$\varepsilon = \varepsilon_0 \left[\frac{f_{\rm c} - f}{f_{\rm c}} \right]^{-s'} \tag{2}$$

where ε_0 is the initial dielectric constant of the pristine Ecoflex, f is the weight fraction of the second phase, and f_c is the corresponding percolation threshold. The solid red curve in Fig. 2c shows the fitting result using eqn (2), and the fitted values of f_c for LMEFS is 0.7 and the corresponding s' is 0.865. The derived value for s' falls within a reasonable range (0.8–1) for a binary system.³⁷ Therefore, according to the definition of the percolation threshold, ε_{SDS} should reach the maximum when the LMP wt% is 70%. This is, however, contradictory to the experimental results shown in Fig. 2b and c which indicate an actual percolation threshold value of \sim 50%. Such a discrepancy can be understood as follows.

It is known that the dielectric constant of a binary system is closely related to the geometrical factor and the spatial distribution of the second-phase additives.32 We run the selected area particle analysis on LMEFS (see the Methods), and the statistical result shown in ESI Fig. 6b† suggests a positive correlation between the LMP wt% and the percentage of the projected area occupied by LMPs inside the silicone matrix. However, when the LMP concentration increases from 50% to 70%, there is no significant change in the percentage of the projected occupied area, indicating that the spatial distribution of LMPs should not be the main factor affecting the dielectric properties of the SDS. Furthermore, ε_{SDS} shows a frequency-independent characteristic (ESI Fig. 5a†), suggesting that the microcapacitor-structure model (MSM)32,38-40 widely adopted for the near-percolationthreshold dielectric constant could be applied to understand the effect of the LMPs' geometrical factor on ε_{SDS} . Within a certain range (from 5 wt% to 50 wt%), the increased wt% of LMP leads to the dispersion of more LMPs and a decreasing distance (ESI Fig. 6a and c†) between adjacent LMPs. According to the MSM theory, 40 such changes lead to a higher ε_r . When the

LMP concentration reaches 70 wt%, the amount of LMPs is expected to continue increasing, and the distance between adjacent LMPs should decrease further. However, the centrifugal force induced in the fabrication and the mechanical pressing²⁶ from CE during the contact-separation TENG process is likely to lead to the fusion of smaller LMPs into larger LMPs. This fusion process is confirmed in ESI Fig. 6b† which shows that the number of LMPs decreases by 40% while the LMP concentration increases from 50 wt% to 70 wt%. Moreover, the statistical result of the primary radius distribution for different LMEFS materials (ESI Fig. 6d†) suggests that LMPs with a larger primary radius (>250 μm) only appear in LMEFS materials with 70 wt% LMP. Thus, even though the distance between adjacent LMPs does not vary significantly (ESI Fig. 6c†), the reduced amount of LMPS inside the Ecoflex matrix leads to a smaller ε_{SDS} . Finally, the measured dissipation factor (D), which evaluates the dielectric material's capability to store charge, for the SDS (50 wt% LMP) is smaller than that for the pristine Ecoflex matrix in the low-frequency range (ESI Fig. 5b†), similar to previous reports.28 This observation is in sharp contrast to previous reports for other known high-k polymers,41 which generally show an increased dissipation factor when the dielectric constant increases.42 Our result suggests that LMEFS could be a promising candidate for future applications such as energy storage devices and smart skins43 where both a high-k and low dissipation factor are needed.20

The operation mechanism of the LMI-TENG and the role of surface leakage charge

To bridge the gap between the KPFM data and TENG output performance, we further studied the electrostatic induction within the SDS and BE. The effect of this electrostatic induction on the TENG performance has been ignored in previous studies under ideal open circuit conditions. 14,44 The general expression for the TENG output voltage is:44

$$V = \frac{\sigma x(t)}{\varepsilon_0} - \frac{Q}{S\varepsilon_0} \left(x(t) + \frac{d_{SDS}}{\varepsilon_{SDS}} \right)$$
 (3)

where σ is the triboelectric charge density on the CL surface, Q is the number of transferred charges between the BE and RE, and $d_{\rm SDS}$ and $\varepsilon_{\rm SDS}$ represent the thickness and dielectric constant of the SDS, respectively. S is the contact area, x(t) is the time-dependent gap distance between the top surface of the CL and RE, and ε_0 is the vacuum dielectric constant. Previous models assume that there is no charge transfer between the BE and RE (Q=0) under open-circuit conditions,²⁴ and the ideal $V_{\rm oc}$ is hence given by:

$$V_{\rm oc} = \frac{\sigma x(t)}{\varepsilon_0} \tag{4}$$

Such an ideal model leads to a trivial electrical field inside the $\rm SDS^{24}$ and the widely accepted understanding that the effective way to boost $V_{\rm oc}$ is to increase the surface charge density through approaches such as modulating the surface roughness of the CL, increasing the dielectric constant of the

SDS, etc18,29. However, in reality, the TENG has a finite dimension, and the electrical field originating from the RE will not terminate at the air-CL interface as assumed in previous models.44 Therefore, there should be negative induction charges accumulated in the BE due to the penetration of the electrical field (E_{air}) through the SDS, where E_{air} is between the RE and the top surface of the SDS. E_{air} thus gives rise to the formation of a nontrivial electrical field (E'_{SDS}) which has the opposite direction to E_{air} (Fig. 3a). As a result, the hypothetical condition Q = 0 is not satisfied, suggesting that a more practical model considering the electrostatic induction in the dielectric layer should be adopted.45 Here, we present an analysis for our proposed model considering the LMEFS-dependent non-trivial electrical field within the SDS (E'_{SDS}) . The modified effective electrical field (E'), which determines V_{oc} , in the TENG under open-circuit conditions should therefore be:

$$E' = \frac{1}{S\varepsilon_0} \left(\sigma S - \frac{Q'}{\varepsilon_{\text{SDS}}} \right) \tag{5}$$

where Q' is the induced charge in the BE (Fig. 3a) by the propagating E_{air} through the SDS. Consequently, Q' can be considered as the "surface leakage charge" during the TENG operation. To the best of our knowledge, the role of such surface leakage charge has not been studied in previous experimental studies.

According to eqn (5), if the dielectric constant of the SDS $(\varepsilon_{\text{SDS}})$ increases, E' will also increase, leading to a boosted V_{oc} . If ε_{SDS} is infinite, E' will be equal to σ/ε_0 , the same as the case for the infinitely large parallel plate capacitor, which is the fundamental model in previous TENG work.44 Finite Element Analysis (FEA) was carried out by using COMSOL Multiphysics to further

verify the correlation between the dielectric constant of the SDS and $E'_{\rm SDS}$. As shown in Fig. 3b, $E'_{\rm SDS}$ decreases when $\varepsilon_{\rm SDS}$ increases, leading to an increased E'. Consequently, the modified expression for the true open-circuit voltage of the TENG should be:

$$V_{\text{oc,true}} = \frac{\sigma x(t)}{\varepsilon_0} - \frac{Q'}{S\varepsilon_0} \left(x(t) + \frac{d_{\text{SDS}}}{\varepsilon_{\text{SDS}}} \right)$$
 (6)

We now turn to the discussion for the short-circuit condition when Q' is included in the model. If the amount of the total transferred charges without Q' is Q_{tr} , the real transferred charges should be Q_{tr} –Q'. Therefore, the output power, which is closely related to the amount of transferred charges between the two electrodes, will decrease accordingly. It should be noted that the magnitude of Q' depends on many factors.24 In our experiment, ε_{SDS} is the main contributor since other factors such as the thickness of the SDS are controlled through the device fabrication. With the increased ε_{SDS} , E'_{SDS} will be largely confined within the SDS, which decreases Q' and results in a higher I_{sc} and Q_{sc} . Since the existence of Q' can significantly affect the TENG performance, more efforts are warranted for a comprehensive evaluation of Q' in future work.

The modified working mechanism for the LMI-TENG can then be understood using the illustrations in Fig. 3c. When the aluminum electrode makes contact with the CL of the SDS, electrons tend to be transferred from the aluminum RE to the CL,46 leaving aluminum positively charged while the top surface of the CL is negatively charged21 (Fig. 3c(i)). Once the two surfaces separate from each other, an electrical field will be established due to the separation of positive and negative charges, driving the flow of electrons from the ITO BE to the

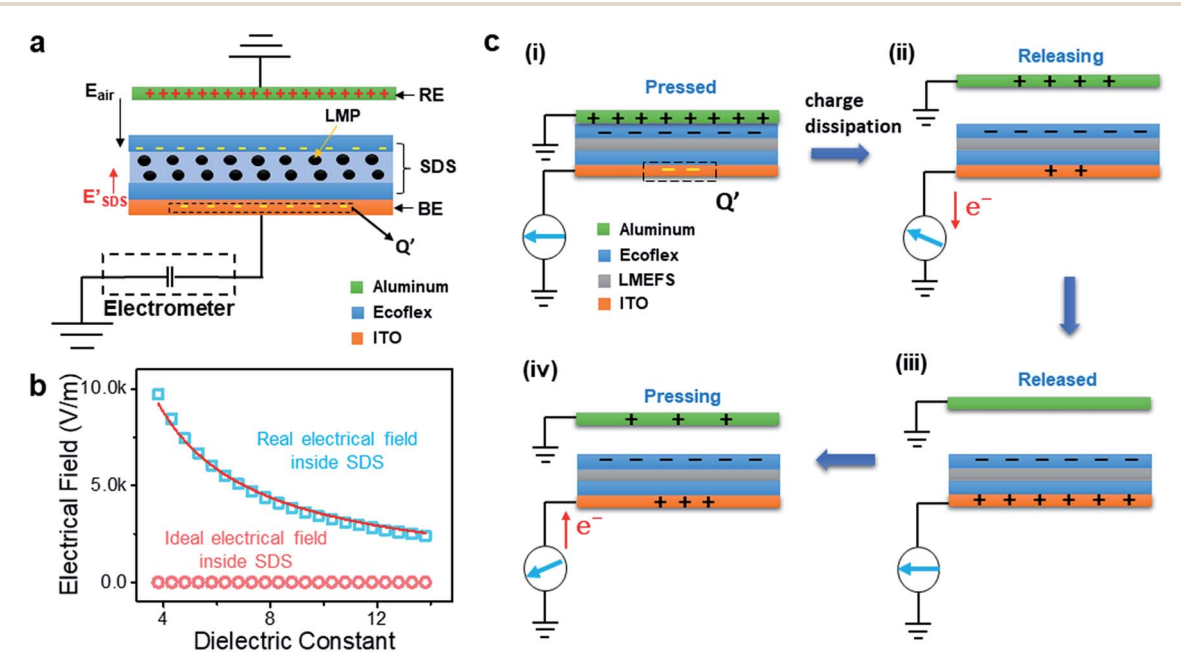


Fig. 3 Electrostatic interaction in LMI-TENG considering the effect of surface leakage charges. (a) Schematic illustration of the electrostatic induction and charge distribution within the SDS and BE. (b) FEA result of the electrical field as a function of the dielectric constant in the SDS. (c) The illustration of the modified TENG working mechanism for the LMI-TENG.

ground (Fig. 3c(ii)). In the meantime, the leakage charge within the BE (Fig. 3c(i)) due to the imperfect screening will dampen the electron transfer and thus affect the V_{oc} (Fig. 3c(ii)). With the increased distance between the aluminum and the CL, the resultant open-circuit voltage (V_{oc}) , short-circuit current density (J_{sc}) , and density of transferred charge between the two electrodes (σ_{sc}) all increase monotonically until a maximum gap distance is reached24 (Fig. 3c(iii)). Subsequently, when the aluminum electrode moves towards the CL, the established electrical field within the LMI-TENG will decrease (Fig. 3c(iv)), resulting in the flow of electrons back to the BE to reach an electrostatic equilibrium.9

Prototypical demonstration of a self-powered user interface

We further designed and demonstrated a stretchable LMI-TENG device, with spray-coated silver nanowires (see ESI Fig. 7† and the Methods) as the BE. The incorporation of silver-nanowire electrodes significantly improves the mechanical stretchability and stability of the LMI-TENG, with no significant degradation in both the electrode conductivity and device output performance after 4500 cycles of the stretch-release test (a maximum strain of 100%) (Fig. 4a). Compared to the LMI-TENG devices with 0 wt% LMP, the output performance of the LMI-TENG with

50 wt% LMP is boosted with an enhancement of 300% (ESI Fig. 8a-c†), consistent with the results shown in Fig. 2c when ITO electrodes are used. More significantly, the stretchable LMI-TENG shows great potential to efficiently harvest mechanical energy at a low frequency (e.g., 0.8 Hz), 47-50 which is important for human-integrated applications as well as harvesting largerscale mechanical energy, e.g., ocean waves.51

The feasibility of our wearable LMI-TENG for potential application in human-integrated technology, e.g., a user interface, 13,25 has been explored. We demonstrated a stretchable LMI-TENG based wireless media control system (MCS) (Fig. 4b and ESI Fig. 9a†). The device can adhere to the human skin comfortably without using a tape (Fig. 4b). The high stretchability of Ecoflex silicone and the silver-nanowire BE ensures that our device can withstand various types of deformation caused by the finger/skin motion during daily operation. The LMI-TENG possesses a good sensitivity in the low-pressure region (ESI Fig. 9b†), promising for human motion detection. 25,52 Our prototypical device consists of three digitized LMI-TENG units (#0, #1, and #2), and the data acquisition interface is realized using a 10-bit analog-to-digital converter (ADC) (ESI Fig. 9c† and the Methods). The adoption of serial communication enables the monitoring of the MCS working status (ESI

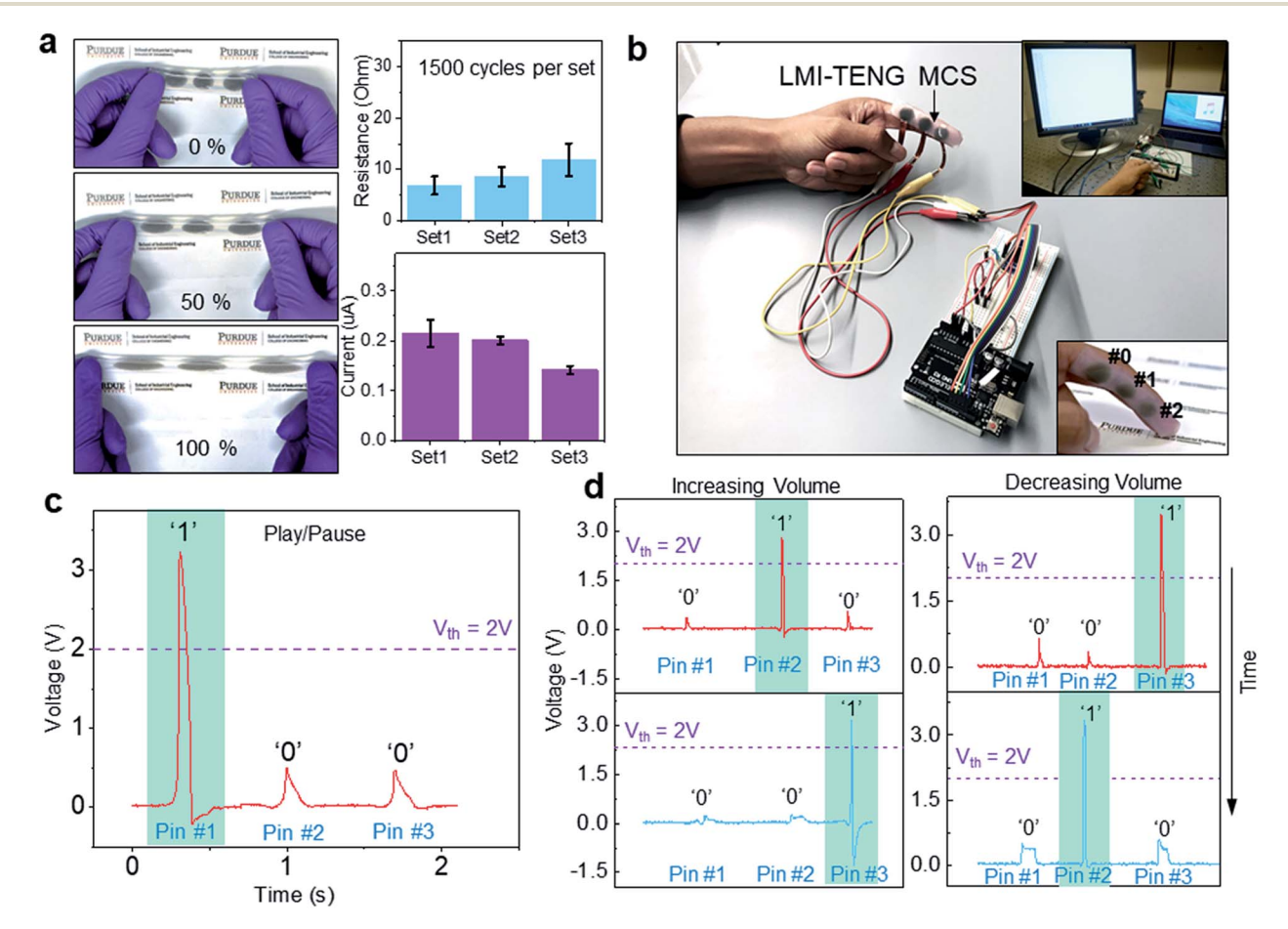


Fig. 4 LMI-TENG for self-powered user interface application. (a) The stretchability test of the LMI-TENG with a Ag NW electrode. (b) Optical image of the wearable LMI-TENG MSC. Inset: the illustration of the testing system and a wearable LMI-TENG MSC device. For detailed operations of the MSC please refer to the ESI Video.† (c), (d) The status signals corresponding to different user interface functions achieved in the MCS.

Fig. 9d†). Our LMI-TENG MCS is capable of detecting and encoding different finger motions into electrical signals with distinct patterns for wirelessly controlling a music player on a remote computer (ESI Fig. 9a†). Fig. 4c shows the electrical outputs from the three LMI-TENGs in the MCS when the "Play/ Pause" function is initiated by only touching the unit #0. The setting of the detection threshold (V_{th}) can address the issue of signal interference in a micro-controller unit (MCU)12 by utilizing different logic levels in each unit. Our MCS can detect the finger motion by identifying the change of the logic level combination of each of the three pins in the MCU. When the sequence of logic levels is switched from "0, 0, 0" to "0, 1, 0" to "0, 0, 1", indicating that the finger is sliding from LMI-TENG #2 to #3 (ESI Video†), the system volume will be increased. When the sequence of logic levels is switched from "0, 0, 0" to "0, 0, 1" to "0, 1, 0", the MCS will decrease the system volume (ESI Video†). The electrical signal processed by the MCU is shown in Fig. 4d. Our system provides a controllable and versatile platform for designing and implementing LMI-TENG based wearable devices in various societally pervasive applications including human-machine interface, remote operation, and smart artificial skin.

Conclusion

In conclusion, we present a platform for exploring liquid-metalinclusion based TENGs where deformable core-shell liquid metal inclusions are incorporated into wearable high-dielectricconstant polymers. Our structural design enables co-optimization for dielectric engineering and surface charge density engineering. Through a holistic integration of modeling and experiments, we identify the design parameter space for enabling the LMI-TENG with optimized output and mechanical deformability. The role of the surface leakage charge, a factor ignored by previous TENG studies, has been theoretically and experimentally investigated for the first time, which extends the theoretical framework of the TENG and advances the fundamental understanding of the TENG's design and optimization. The device architecture and design scheme shown here provide a promising solution for optimizing both the TENG devices' wearability and operation performance through cost-effective, scalable approaches. Our work presents an important step towards the realization of self-powered human-integrated technologies.

Methods

Fabrication of LMEFS

A layer of Ecoflex 00-30 (Base & Cure, 1:1 by weight ratio and degassed for 10 minutes) was first coated onto the PET-ITO substrate using a spinner and cured on a hotplate at 60 °C. Then a liquid Ecoflex base was mixed and mechanically stirred with liquid metal (Consolidated Chemical & Solvents) transferred using a pipette for 7 minutes. After this, the composite was mixed with an Ecoflex cure (1:1 by volume ratio), degassed for 10 minutes and cured at 60 °C. Finally, another layer of Ecoflex

was again coated onto the previous layer and cured for another 10 minutes at 60 °C.

Fabrication of LMI-TENGS

For PET-ITO as the back electrode, after the fabrication of LMEFS, a copper wire was inserted on the back of the ITO as the conductive wire connected to the electrical measurement system. For silver nanowires (Ag NWs) as the back electrode, before the fabrication of LMEFS, a layer of Ag NWs was dropcast onto the non-conductive PET side and annealed at 60 °C for 30 minutes. After the annealing, the following steps are the same as the steps in the fabrication of LMEFS. After that, the whole device was peeled off from the PET substrate, a copper tape serving as the conductive wire was connected to the Ag NWs, and another layer of Ecoflex was blade coated over it.

Particles characterization

The optical image was taken using an Olympus BX53M and post-processed by ImageJ. (1) Each raw optical image was converted to a binary image (image → adjust → threshold, with a lower cutoff of ≈ 15 and an upper cutoff of ≈ 230 and the dark background option); (2) each resulting binary image was segmented using the built-in ImageJ watershed routine (process \rightarrow binary \rightarrow watershed); (3) the sizes of all segmented particles were obtained using ImageJ's particle analysis package (analyze → analyze particles, with the size range going from 10 square pixel units to infinity, circularity from 0 to 1, showing a bare outline of particles); (4) the diameter of each particle was computed from the area output by ImageJ in a spherical approximation. The 3D spatial distribution of LMPs inside the Ecoflex matrix was carried out using a Scanco MicroCT u40 and the 3D image was constructed by MeshLab 2016.

TENG characterization and measurement

The output performance of the LMI-TENG was characterized using a SR 570 (Stanford Research Systems) and Keithley 6514 electrometer. KPFM was performed by using a Keysight 5500 AFM in KPFM-AM mode. The dielectric constant was measured by using Keysight B1500A semiconductor device parameters in capacitance-frequency mode. The data communication between the LMI-TENG sensing unit, bluetooth module (Adafruit) and the computer was performed via serial communication from an embedded computing platform (Arduino Uno, Arduino).

Author contributions

W. Z. W. and S. J. G conceived the idea. W. Z. W. designed the experiments and supervised the project. W. Z. W. and S. J. G. analyzed the data and wrote the manuscript. S. J. G. fabricated the LMI-TENG devices and performed the characterization. S. J. G. carried out the FEA simulations. F. R. F. synthesized the silver nanowires and guided the experiments for stretchable electrodes. W. X. W. guided the experiments for LMI engineering. S. J. G. and Z. H. C. performed the prototypical demonstration. R. X. W., C. X. M., Y. X. W., and M. W. provided necessary help during the experiment. All authors have discussed the results and commented on the paper.

Conflicts of interest

The authors declare no competing financial interests.

Acknowledgements

W. Z. W. acknowledges the College of Engineering and School of Industrial Engineering at Purdue University for the startup support. W. Z. W. was partially sponsored by the National Science Foundation under grant CNS-1726865. Part of the device fabrication was supported by a subcontract from the Idaho National Laboratory Directed Research and Development Program under DOE Idaho Operations Office Contract DE-AC07-05ID14517. We thank Pamela Lachcik for the help with Micro-CT operation.

References

- 1 Z. L. Wang and W. Wu, Angew. Chem., Int. Ed., 2012, 51, 11700-11721.
- 2 Q. Zheng, Y. Zou, Y. Zhang, Z. Liu, B. Shi, X. Wang, Y. Jin, H. Ouyang, Z. Li and Z. L. Wang, Sci. Adv., 2016, 2, e1501478.
- 3 L. Atzori, A. Iera and G. Morabito, *Comput. Netw.*, 2010, 54, 2787–2805.
- 4 J. A. Rogers, T. Someya and Y. Huang, *Science*, 2010, 327, 1603–1607.
- 5 W. Gao, S. Emaminejad, H. Y. Y. Nyein, S. Challa, K. Chen, A. Peck, H. M. Fahad, H. Ota, H. Shiraki and D. Kiriya, *Nature*, 2016, 529, 509.
- 6 Z. L. Wang, Mater. Today, 2017, 20, 74-82.
- 7 F.-R. Fan, Z.-Q. Tian and Z. Lin Wang, *Nano Energy*, 2012, 1, 328–334.
- 8 Y. Zi, J. Wang, S. Wang, S. Li, Z. Wen, H. Guo and Z. L. Wang, *Nat. Commun.*, 2016, 7, 10987.
- 9 Z. L. Wang, ACS Nano, 2013, 7, 9533-9557.
- 10 F.-R. Fan, L. Lin, G. Zhu, W. Wu, R. Zhang and Z. L. Wang, *Nano Lett.*, 2012, **12**, 3109–3114.
- 11 S. Wang, L. Lin and Z. L. Wang, *Nano Energy*, 2015, **11**, 436–462.
- 12 J. Chen, G. Zhu, J. Yang, Q. Jing, P. Bai, W. Yang, X. Qi, Y. Su and Z. L. Wang, *ACS Nano*, 2015, **9**, 105–116.
- 13 C. Wu, W. Ding, R. Liu, J. Wang, A. C. Wang, J. Wang, S. Li, Y. Zi and Z. L. Wang, *Mater. Today*, 2018, **21**(3), 216–222.
- 14 W. Seung, H. J. Yoon, T. Y. Kim, H. Ryu, J. Kim, J. H. Lee, J. H. Lee, S. Kim, Y. K. Park and Y. J. Park, *Advanced Energy Materials*, 2016.
- 15 J. Chen, H. Guo, X. He, G. Liu, Y. Xi, H. Shi and C. Hu, *ACS Appl. Mater. Interfaces*, 2015, **8**, 736–744.
- 16 Y. Yu, Z. Li, Y. Wang, S. Gong and X. Wang, *Adv. Mater.*, 2015, 27, 4938–4944.
- 17 S. Wang, Y. Xie, S. Niu, L. Lin, C. Liu, Y. S. Zhou and Z. L. Wang, *Adv. Mater.*, 2014, **26**, 6720–6728.
- 18 N. Cui, L. Gu, Y. Lei, J. Liu, Y. Qin, X. Ma, Y. Hao and Z. L. Wang, *ACS Nano*, 2016, **10**, 6131–6138.

- 19 J. Chun, J. W. Kim, W.-s. Jung, C.-Y. Kang, S.-W. Kim, Z. L. Wang and J. M. Baik, *Energy Environ. Sci.*, 2015, 8, 3006–3012.
- 20 J. Lu and C. Wong, *IEEE Trans. Dielectr. Electr. Insul.*, 2008, **15**, 1322–1328.
- 21 Y. C. Lai, J. Deng, S. Niu, W. Peng, C. Wu, R. Liu, Z. Wen and Z. L. Wang, *Adv. Mater.*, 2016, 28, 10024–10032.
- 22 J. Wang, S. Li, F. Yi, Y. Zi, J. Lin, X. Wang, Y. Xu and Z. L. Wang, *Nat. Commun.*, 2016, 7, 12744.
- 23 J. Wang, C. Wu, Y. Dai, Z. Zhao, A. Wang, T. Zhang and Z. L. Wang, *Nat. Commun.*, 2017, 8, 88.
- 24 S. Niu, S. Wang, L. Lin, Y. Liu, Y. S. Zhou, Y. Hu and Z. L. Wang, *Energy Environ. Sci.*, 2013, **6**, 3576–3583.
- 25 X. Pu, H. Guo, J. Chen, X. Wang, Y. Xi, C. Hu and Z. L. Wang, *Sci. Adv.*, 2017, 3, e1700694.
- 26 J. W. Boley, E. L. White and R. K. Kramer, Adv. Mater., 2015, 27, 2355–2360.
- 27 M. D. Dickey, R. C. Chiechi, R. J. Larsen, E. A. Weiss, D. A. Weitz and G. M. Whitesides, *Adv. Funct. Mater.*, 2008, 18, 1097–1104.
- 28 M. D. Bartlett, A. Fassler, N. Kazem, E. J. Markvicka, P. Mandal and C. Majidi, *Adv. Mater.*, 2016, 28, 3726–3731.
- 29 Z. L. Wang, J. Chen and L. Lin, Energy Environ. Sci., 2015, 8, 2250–2282.
- 30 Z. Fang, K. H. Chan, X. Lu, C. F. Tan and G. W. Ho, *J. Mater. Chem. A*, 2018, **6**, 52–57.
- 31 S. Cheon, H. Kang, H. Kim, Y. Son, J. Y. Lee, H. J. Shin, S. W. Kim and J. H. Cho, Adv. Funct. Mater., 2018, 28(2), 1703778.
- 32 C.-W. Nan, Y. Shen and J. Ma, *Annu. Rev. Mater. Res.*, 2010, **40**, 131–151.
- 33 Y. Zi, S. Niu, J. Wang, Z. Wen, W. Tang and Z. L. Wang, *Nat. Commun.*, 2015, **6**, 8376.
- 34 W. Melitz, J. Shen, A. C. Kummel and S. Lee, *Surf. Sci. Rep.*, 2011, **66**, 1–27.
- 35 L. Flandin, T. Prasse, R. Schueler, K. Schulte, W. Bauhofer and J.-Y. Cavaille, *Phys. Rev. B: Condens. Matter Mater. Phys.*, 1999, **59**, 14349.
- 36 C. C. Wang, J. F. Song, H. M. Bao, Q. D. Shen and C. Z. Yang, *Adv. Funct. Mater.*, 2008, **18**, 1299–1306.
- 37 L. Wang and Z.-M. Dang, Appl. Phys. Lett., 2005, 87, 042903.
- 38 X. Zeng, L. Deng, Y. Yao, R. Sun, J. Xu and C.-P. Wong, *J. Mater. Chem. C*, 2016, **4**, 6037–6044.
- 39 R. Simoes, J. Silva, R. Vaia, V. Sencadas, P. Costa, J. Gomes and S. Lanceros-Méndez, *Nanotechnology*, 2008, **20**, 035703.
- 40 C. Pecharromán and J. S. Moya, *Adv. Mater.*, 2000, **12**, 294–297.
- 41 Z.-M. Dang, J.-K. Yuan, J.-W. Zha, T. Zhou, S.-T. Li and G.-H. Hu, *Prog. Mater. Sci.*, 2012, 57, 660–723.
- 42 J. Lu, K.-S. Moon, J. Xu and C. Wong, *J. Mater. Chem.*, 2006, **16**, 1543–1548.
- 43 L. Zhu, J. Phys. Chem. Lett., 2014, 5, 3677-3687.
- 44 S. Niu and Z. L. Wang, Nano Energy, 2015, 14, 161-192.
- 45 R. D. I. G. Dharmasena, K. Jayawardena, C. Mills, J. Deane, J. Anguita, R. Dorey and S. Silva, *Energy Environ. Sci.*, 2017, **10**, 1801–1811.

- 46 C. Xu, Y. Zi, A. C. Wang, H. Zou, Y. Dai, X. He, P. Wang, Y.-C. Wang, P. Feng, D. Li and Z. L. Wang, *Adv. Mater.*, 2018, **30**(15), 1706790.
- 47 Y. Zi, H. Guo, Z. Wen, M.-H. Yeh, C. Hu and Z. L. Wang, *ACS Nano*, 2016, **10**, 4797–4805.
- 48 F. Xing, Y. Jie, X. Cao, T. Li and N. Wang, *Nano Energy*, 2017, **42**, 138–142.
- 49 Y. Yuan, H. Zhang, J. Wang, Y. Xie, S. A. Khan, L. Jin, Z. Yan, L. Huang, T. Pan and W. Yang, *Materials Research Express*, 2018.
- 50 X. Wang, S. Niu, Y. Yin, F. Yi, Z. You and Z. L. Wang, *Adv. Energy Mater.*, 2015, 5(24), 1501467.
- 51 J. Chen, J. Yang, Z. Li, X. Fan, Y. Zi, Q. Jing, H. Guo, Z. Wen, K. C. Pradel and S. Niu, ACS Nano, 2015, 9, 3324–3331
- 52 Y. Yang, H. Zhang, Z.-H. Lin, Y. S. Zhou, Q. Jing, Y. Su, J. Yang, J. Chen, C. Hu and Z. L. Wang, ACS Nano, 2013, 7, 9213–9222.